Improved Core Fueling with High Field Side Pellet Injection in the DIII-D Tokamak

L.R. Baylor, T.C. Jernigan, S.K. Combs, W.A. Houlberg, M. Murakami

Oak Ridge National Laboratory, Oak Ridge, TN.

P. Gohil, K.H. Burrell, C.M. Greenfield, R.J. Groebner, C.-L. Hsieh, R.J. La Haye, P.B. Parks, G.M. Staebler, and The DIII-D Team

General Atomics, San Diego, CA.

G.L. Schmidt, D.R. Ernst, E.J. Synakowski

Princeton Plasma Physics Laboratory, Princeton, NJ.

M. Porkolab

Massachusetts Institute of Technology, Cambridge, MA.

(November 23, 1999)

Abstract

The capability to inject deuterium pellets from the magnetic high field side (HFS) has been added to the DIII-D tokamak [J. L. Luxon and L. G. Davis, Fusion Technol. **8**, 441 (1985)]. It is observed that pellets injected from the HFS lead to deeper mass deposition than identical pellets injected from the outside midplane, in spite of a factor of 4 lower pellet speed. HFS injected pellets have been used to generate peaked density profile plasmas [peaking factor $(n_e(0)/\langle n_e \rangle)$ in excess of 3] that develop internal transport

barriers when centrally heated with neutral beam injection. The transport barriers are formed in conditions where $T_e \sim T_i$ and $q(0)$ is above unity. The peaked density profiles, characteristic of the internal transport barrier, persist for several energy confinement times and survive through L-mode to H-mode transitions. The pellets injected from the different locations are also used as probes to investigate transport barrier physics and modify plasma edge conditions. Transitions from L- to H-mode have been triggered by pellets from both the HFS and low field side (LFS), effectively lowering the H-mode threshold power by 2.4 MW. Pellets injected into H-mode plasmas are found to trigger edge localized modes (ELMs). ELMs triggered from the LFS outside midplane injected pellets are of significantly longer duration than from HFS injected pellets.

Valid PACS appear here. \pacs{}

Typeset using REVTEX

I. INTRODUCTION

Pellet injection is an important technique used for fueling and density profile control in magnetically confined plasmas that has been investigated for many years [1]. Much effort in past pellet fueling experiments has been devoted to understanding pellet ablation and pellet induced changes in plasma transport. A versatile repeating pneumatic pellet injector with three independent barrels, which was designed and built for earlier Joint European Torus (JET) experiments, was installed on DIII-D to study fueling and transport in a highly shaped tokamak [2].

The density profile modification from pellet injection in JET and Tokamak Fusion Test Reactor (TFTR) experiments was shown to disagree with conventional pellet ablation theory that assumes the pellet particles remain on the field lines where they are ionized [3]. The penetration depth of pellets injected in many machines over a wide range of plasma conditions measured by the duration of the pellet light emission agreed well with pellet ablation theory. This suggested that a fast outward radial transport may occur during the pellet ablation and toroidal symmetrization processes. The first experiment to test this hypothesis and attempt high field side (HFS) pellet injection was on ASDEX-Upgrade [4], which showed improved fueling efficiency with small low-speed HFS injected pellets. Detailed measurement of an outward radial particle deposition from low field side (LFS) injected pellets was shown on DIII-D, and deeper than expected central deposition from vertical pellet injection was observed [5]. The recent observations of a fast outward radial plasma drift from LFS injected pellets on RTP [6] and from HFS injected pellets on ASDEX-Upgrade [7] support the hypothesis of an outward radial drift of the pellet ablatant.

To utilize the HFS pellet injection technique on DIII-D for enhanced core fueling, two stainless steel guide tubes were installed inside the DIII-D vacuum vessel behind tiles on the inner wall. The tubes exit on the midplane and 30 cm above the midplane angled toward the magnetic axis. Curved stainless steel guide tubes connect the inner wall tubes to the pellet injector, making it possible to inject pellets from the inner wall (HFS), outer midplane

(LFS), and a vertical port inside the magnetic axis with the three guns on the DIII-D pellet injector.

In Sec. II of this paper we further describe the experimental configuration and discuss the observations of core fueling from the different pellet injection locations. Deep core fueling is observed with pellets injected from the HFS inner wall guide tubes. The resulting particle deposition is significantly deeper than from identical-size pellets launched from the LFS outer midplane, in spite of having a factor of 4 slower speed than LFS outside midplane launched pellets. This observation is consistent with the hypothesis that a fast major radius drift of the pellet mass occurs during the distribution process in the plasma. In Sec. III we present the results of experiments that use pellets as tools to induce changes in core transport, both in internal transport barrier formation and in transitions to H-mode operation. Pellets injected from the HFS can produce very peaked density profiles that lead to internal transport barrier formation with strong central heating. The first measurement of the radial electric field in these pellet enhanced performance (PEP) mode plasmas shows that $\mathbf{E} \times \mathbf{B}$ shear stabilizes the ion temperature gradient mode in these plasmas. In Sec. IV we present a description of the results of pellet interaction with the edge plasma, in particular the triggering of edge localized modes (ELMs). The ELMs triggered from pellets injected from the HFS inner wall and vertical injection ports are similar to the background ELMs in magnitude and duration. ELMs triggered from LFS outer midplane injected pellets are of significantly longer duration and lead to poor fueling efficiency and lower energy confinement. Finally, in Sec. V we present a summary of our main conclusions from this work.

II. CORE FUELING

The layout of the pellet injection ports in a poloidal cross section of the DIII-D tokamak injection ports are shown in Fig. 1. The HFS injection locations are at different toroidal locations from the vertical port and LFS port. The inner wall guide tubes were designed to maximize the bend radii to allow high speed pellets to be transmitted intact. The pellets

can survive the transit to the plasma intact if the shear stress of the pellet ice is not exceeded by cumulative collisions in the guide tube or the centrifugal force does not exceed the shear stress of the ice. Tests of the designed tubes were made and showed that pellet speeds of up to 300 m/s could survive the trajectory without significant degradation in pellet integrity [8]. In the experiment the pellet speed was found to decrease by $1-2\%$, based on time-of-flight measurements from the pellet light gates diagnostics near the end of the injector barrels and the measured D_α emission of the pellet in the plasma.

Direct comparisons of plasma response to pellets injected from different locations into the same plasma discharge are possible with the three independent guns on the DIII-D pellet injector. Fig. 2 shows an example where the same size pellets (2.7 mm diameter at formation) were injected at different speeds from the HFS 45, V+1, and LFS locations in a neutral beam heated L-mode plasma. The density perturbation from the HFS injected pellet is clearly greater as shown by the line average density measurement of the central interferometer chord even though the pellet speed is a factor of 4 slower. The D_α light measured in the divertor shows a large increase with the LFS injected pellet, which indicats that mass from the pellet is immediately expelled from the plasma. The HFS injected pellet does not cause very much change in the divertor D_α level, which indicates efficient fueling by the pellet.

The particle deposition of injected pellets is determined by the measured density profiles before and after injection of the pellet. On DIII-D this is accomplished with the multipoint Thomson scattering diagnostic that measures the electron density profile every 12.5 ms. Density profiles measured immediately after pellet injection show pellet mass deposited beyond the penetration radius for the HFS injected pellets, which supports the hypothesis that a drift of the pellet ablatant occurs in the major radius direction. Pellets injected from the LFS show shallower mass deposition than the HFS or vertical pellets in spite of much higher pellet speeds. Fig. 3 shows an example of the measured particle deposition profiles from HFS and LFS injected pellets into the same discharge under the same conditions. The density profile change from the HFS injected pellet is observed to extend much deeper than

the calculated penetration depth of the pellet, while the density change from the LFS pellet is skewed toward the plasma boundary as was observed previously [5].

The penetration depth of the pellets λ has been determined from the duration of the D_α emission of the ablating pellet, assuming that the radial velocity of the pellet does not change. We have used the measured pellet speed from light barriers at the end of the barrels, the pellet mass from a microwave cavity, along with the measured plasma electron temperature and density profiles, and the actual plasma geometry to model the pellet ablation process using the neutral gas shielding (NGS) model in the PELLET code [9], which was used to model pellet penetration results from JET [10]. The calculated penetration depth of the pellets is shown as arrows in Fig. 3. The pellets injected from both HFS inner wall ports and from the V+1 port result in deeper density perturbations than calculated from the model, while the maximum depth of the density perturbation from LFS injected pellets agrees reasonably well with the model.

In Fig. 4 we show the particle deposition profile for a HFS pellet injected into an H-mode plasma. The deposition profile that is calculated from the NGS model using the PELLET code and the pellet ablation light mapped onto flux surface geometry are also shown. The ablation light emission and calculated deposition profile show similar penetration depths. However, the measured deposition is much deeper than calculated as also seen in Fig. 3. It does not seem likely that the discrepancy in deposition from ablation theory can be explained by toroidal deflection of the pellet nor diffusion because the measured deposition is only 0.25 ms after the end of ablation of the pellet.

The light emission from ablating pellets shows striations in the emission intensity that are thought to be caused by a rotation instability in the pellet cloud [11]. Striations are observed in the HFS and vertical injected pellets with no qualitative difference from the LFS injected pellets, which leads us to believe that the cloud instability is not strongly affected by the increased magnetic field inside the magnetic axis.

The fueling efficiency, defined as the fraction of pellet mass that is retained in the plasma, is higher for the HFS injected pellets than the LFS injected pellets. It approaches 95% or

greater if the pellet mass loss in the curved guide tube is taken into account. The LFS injected pellets have been shown [12] to have a fueling efficiency inversely dependent on heating power, dropping to under 50% with 10 MW of heating power. The LFS pellet fueling efficiency is especially poor in H-mode plasmas where higher edge temperatures and shallower pellet penetration depths are encountered. The deposition profiles from Fig. 3, when integrated, yield a fueling efficiency of 95% for the HFS injected pellet and 55% for the LFS injected pellet.

The mechanism responsible for the apparent drift of pellet ablatant in the major radius direction is hypothesized to be caused by an $\mathbf{E} \times \mathbf{B}$ drift that arises from a vertical polarization of the ionized part of the ablation cloud due to $\nabla\mathbf{B}$ and curvature-induced charged particle drifts [13]. The timescale for such drifts on DIII-D are on the order of tens of microseconds. The ablatant would be expected to move in the $\nabla\mathbf{B}$ (outward major radius) direction independent of injection location. Some portion of the pellet ablatant is thought to propagate 10 cm or more in the $\nabla\mathbf{B}$ direction and is actually expelled from the plasma confinement region for LFS pellets, thus reducing the fueling efficiency. The measured increase in divertor D_α emission following a LFS injected pellet, as shown in Fig. 2, supports this hypothesis.

A detailed model for the large-R drift of the ablated pellet material has been developed by Parks [14]. This model calculates the large-R penetration depth of the pellet ablation cloud as a function of the measured local plasma parameters and calculated pellet cloud parameters given by the following formula in units of eV-cm-T:

$$\Delta R = \frac{4.6 {r_p}^{1/3}}{M_0 \kappa_c B} \frac{{T_e}^{11/6}}{(ln\Lambda_{en})^{2/3}} \left(\frac{W}{n_e}\right)^{1/6} \langle\tilde{\Psi}\rangle, \tag{2.1}$$

where ΔR is the radial drift, r_p is the pellet radius, T_e is the background electron temperature, n_e is the background electron density, κ_c is the cloud radius normalized to the pellet radius, B is the background magnetic field, $M_0 \sim 0.8$ is the Mach number of the ablation flow at the entrance of the field-aligned ablation channel boundary, $ln\Lambda_{en}$ is the Coulomb logarithm for electron-neutral interaction, W is the pellet atomic mass, and $\langle\tilde{\Psi}\rangle$

is a source term for the electrostatic drive that scales as $\sim n_e T_e$ of the background plasma. Using experimental values for the case shown in Fig. 4, $\Delta R = 30\,\mathrm{cm}$ near the end of the pellet trajectory. This is approximately the level of radial displacement needed to explain the observed deposition profile extending beyond the pellet penetration depth. The model, primarily through the electrostatic drive term, predicts stronger displacement as the pellet enters higher β background plasma, so more displacement is predicted the deeper the pellet enters the plasma.

III. TRANSPORT BARRIER FORMATION

The multiple pellet injection locations installed on DIII-D provide a flexible tool that enables pellets to be used as probes to investigate transport barrier physics and modify plasma edge conditions. The deeper mass deposition provided by the HFS injection locations can be used to produce peaked density profiles in conditions where LFS pellets do not penetrate sufficiently to deposit particles in the plasma center. The HFS pellets also have stronger and deeper density perturbations that lead to stronger modification to the local plasma parameters.

Deuterium pellets have been injected into DIII-D plasmas from the HFS during the plasma current rise; this leads to the formation of peaked density profiles with a peaking factor $(n_e(0)/\langle n_e \rangle)$ in excess of 3. The peaked density profile plasmas formed with the HFS injected pellets develop internal transport barriers when centrally heated. The transport barriers are formed in conditions where $T_e \sim T_i$ and $q(r) > 1$ with low negative central shear. The peaked density profiles, characteristic of the internal transport barrier, persist for many energy confinement times and survive through L- to H-mode transitions. When pellets are injected into L-mode plasmas with power below the H-mode threshold, it is possible for the pellet to lead to the formation of an edge transport barrier and trigger an H-mode transition.

A. Internal Transport Barrier: PEP-mode

Pellets were injected during the current rise to study the physics of internal transport barrier (ITB) formation with $T_i \sim T_e$. In the original PEP-mode experiments on JET, ITBs were formed using ion cyclotron resonance heating (ICRH) with reduced transport in both the ion and electron channel [15,16]. The mechanism for the PEP-mode was not well understood because of uncertain measurement of many of the plasma profiles. In these experiments on DIII-D there was complete diagnostic coverage to obtain full kinetic profiles and magnetic configuration in order to investigate the role of $\mathbf{E} \times \mathbf{B}$ shear in the suppression of turbulence in the PEP-mode.

In the PEP experiments either low-power electron cyclotron heating (ECH) or neutral beam injection (NBI) was applied before the pellets were injected to freeze the current profile during the current rise producing a negative central shear configuration. A single HFS pellet when injected into the preheated plasma did not lead to a strong central density peaking as it did in ohmic plasma; therefore, a pellet was injected from the LFS outside midplane just before the HFS pellet to precool the plasma edge. The HFS injected pellet then penetrated deep into the core and produced highly peaked density profile targets. When high-power NBI was applied to the peaked density target, either in or counter to the plasma current direction, an ITB is formed with $T_i \sim 1.25\,T_e$. Without using pellet injection, the ITB forms in DIII-D in a hot ion mode with $T_i \gg T_e$ [17]. Fig. 5 shows the temporal evolution for a typical PEP-mode ITB discharge. The ITB forms in this case 150 ms after the high-power counter-NBI is turned on.

Central particle deposition by the pellet is needed for the formation of the PEP-mode on DIII-D as has been observed on other tokamaks [**?**,18]. HFS pellet injection leads to deeper particle deposition, especially when used just after a LFS pellet for edge precooling. No magnetohydrodynamic (MHD) activity (such as frequently observed locked-modes) is instigated by the pellet injection during the current rise. Pellets injected later during the current flattop with positive magnetic shear do not lead to PEP-mode ITB conditions. In

TFTR PEP experiments where the pellets were injected in the current flattop with low central shear, a weak ITB was formed [18].

In these PEP discharges the radial electric field is calculated by radial force balance analysis, using the carbon impurity ion temperature, density, and poloidal and toroidal rotation velocities, all measured by charge exchange recombination spectroscopy [19]. The magnetic field components and safety factor q were obtained from the EFIT equilibrium reconstruction code [20], constrained by motional Stark effect (MSE) measurements of the vertical magnetic field, corrected for the local electric field [21]. TRANSP [22] is used to determine the power balance and infer thermal and particle diffusivities from the measured profiles of temperature, electron and carbon density, and radiated power. The measured profiles of temperature, density, and safety factor (q) are shown in Fig. 6 for the PEP-mode discharge shown in Fig. 5.

The pressure gradient driven neoclassical bootstrap current (J_{BS}) is calculated from the NCLASS code [23] within TRANSP. The PEP-mode discharges show a large off-axis bootstrap current, which sustains and develops stronger negative central shear than in non-PEP ITB comparison discharges. Fig. 7 shows the calculated bootstrap current for a PEP ITB and a comparison non-PEP ITB plasma. The q profiles are also shown for these cases; it is apparent that the off-axis bootstrap current results in stronger negative central shear. This implies that the strong pressure gradient at the ITB in the PEP-mode acts as feedback to maintain the strong negative central shear at the foot of the ITB. No sawtooth activity is present in these discharges to support the q profile measurements that show $q > 1$ everywhere.

Transport results from TRANSP analysis are shown in Fig. 8 for the PEP ITB discharge and comparison non-PEP ITB discharge shown in Fig. 5. Both the ions and electrons have low thermal diffusivities that approach ion neoclassical levels in the core where the strong gradient region exists. There is not a significant difference outside the error bars in the diffusivity calculations between the PEP ITB and non-PEP ITB cases. There is reduced electron particle transport in the PEP ITB compared to non-PEP ITB discharge.

In these pellet-enhanced ITB plasmas, the toroidal rotation profile of the carbon shows a notch feature with co-NBI heating and a nib or antinotch feature with counter-NBI heating. Fig. 9(a) shows examples of the measured carbon rotation profiles with these features. A similar notch was first observed in carbon rotation profiles in TFTR supershot plasmas and was explained by neoclassical parallel momentum transfer [24]. The same mechanism is thought to be responsible for this feature observed in the PEP ITB plasmas. Calculated deuterium rotation profiles from neoclassical calculation by NCLASS show a monotonic profile as shown in Fig. 9(a). This is expected because the anomalous momentum transport is considered to be diffusive in nature. The rotation notch feature has not been observed in non-PEP ITB plasmas.

The radial electric field profile has a well structure for the co-NBI and counter-NBI PEP cases. The well is located at the foot of the ITB and at the notch in the rotation profile. The radial electric field is determined from the radial force balance for the measured carbon profiles given by the following equation:

$$E_r = \frac{\nabla P_i}{Z_i e n_i} + v_{\phi i} B_\theta - v_{\theta i} B_\phi, \tag{3.1}$$

where P_i is the pressure for species i, and $v_{\phi i}$ and $v_{\theta i}$ are the toroidal and poloidal velocities for species i. E_r is the same for all species, but individual terms of course are not. The radial electric field profile and its components from the previous equation are shown for these co- and counter-NBI cases in Fig. 9(b) and (c). The toroidal rotation term has a deep well at the location of the notch and well in E_r. The PEP ITB plasmas have a stronger pressure gradient, but higher density than the non-PEP ITB comparison such that the ∇P_i contribution to the radial electric field is not significantly different. Direct measurement of the radial electric field is made by MSE diagnostic and qualitatively agrees with the force balance E_r. However, the error bars for the MSE measurement are of the order of the measured level.

An associated shear layer located at this E_r well provides the coupling between the ion temperature gradient and the radial electric field. The transport behavior appears consistent

with the paradigm of microturbulence stabilization by $\mathbf{E} \times \mathbf{B}$ shear flow [25] that has been shown to be consistent with barrier formation in other DIII-D ITB plasmas [26,27]. The $\mathbf{E} \times \mathbf{B}$ shearing rate is calculated from the following equation:

$$\omega_{E\times B} = \frac{(RB_\theta)^2}{B} \frac{\partial}{\partial \psi} \left(\frac{E_r}{RB_\theta} \right). \tag{3.2}$$

This shearing rate can be compared to theory-based predictions of microturbulence growth using a 3-D ballooning mode linear gyrokinetic stability code in the electromagnetic limit [28] that has been modified for noncircular geometry [29]. In these calculations the maximum growth rate $\gamma_{\max}$ is computed as the larger of the growth rates of the ion temperature gradient (ITG) and dissipative trapped electron modes (TEMs).

In Fig. 10 we compare the shearing rate and calculated growth rates for the PEP ITB conditions presented. For the low-k ITG mode, $\omega_{E\times B} \geq \gamma_{\max}$ for $\rho < 0.5$; this indicates agreement between the region of calculated suppression of low-k turbulence and the region with reduced transport for the ions. Inside of $\rho \sim 0.45$, which is the location of the foot of the ITB, the ITG mode is stabilized. Outside of $\rho \sim 0.5$, a TEM has a growth rate that exceeds $\omega_{E\times B}$.

A transition to H-mode occurs relatively soon in these PEP ITB discharges. The H-mode is characterized by a low-density pedestal value and rapid small ELMs. The energy confinement is about 20% above L-mode. The ELMs are weak and localized at the plasma edge and do not affect the ITB in these PEP discharges. The H-mode has a low pedestal density that allows good NBI penetration, but does not lead to particularly good H-mode confinement as was the case in the earlier JET PEP H-mode discharges [16].

The carbon density, which is the dominant impurity, is observed to increase in the core during the PEP phase. It is expelled at the collapse of the PEP ITB. Accumulation of higher Z impurities is expected due to neoclassical ∇n inward convection. The neoclassical temperature screening due to ∇T_i outward convection is not as strong as in other DIII-D ITB hot ion regime plasmas.

The PEP-mode termination in DIII-D occurs some 0.3 to 1.1 s into the heating period.

The termination usually occurs with a rapid collapse of central pressure as in similar experiments on JET [15]. Sawteeth do not terminate the mode as on JT-60 and are not observed during the enhanced performance phase. The PEP-mode termination correlates with the appearance of MHD activity that is characterized as an $n = 1$ oscillation with a very fast ($< 1\,\mathrm{ms}$) growth rate. This MHD mode leads to the collapse of peaked central density and pressure. Neutrons and stored energy drop dramatically at the time of the collapse. The MHD mode has not been identified, but it could be an internal resistive kink or an infernal mode [30]. Pellets injected into existing PEP-mode ITBs were not successful in extending the duration and, in fact, were often responsible for termination of the ITB. Future PEP-mode experiments on DIII-D may use ICRH for stronger central heating and fast wave or electron cyclotron current drive to maintain $q(r) > 2$ and extend the PEP-mode duration.

B. Pellet-Induced H-mode

Pellets injected from both the LFS and HFS on DIII-D have been verified to produce an adiabatic change in the plasma with total plasma pressure conserved within the error bars of the measurements [31]. It has also been observed that the angular momentum of the bulk plasma is conserved when a pellet is injected either from the LFS or HFS. This implies that a pellet can be used to modify the radial electric field at the plasma edge through the toroidal rotation term in Eq. (3.1). Measurements of the radial electric field with the MSE diagnostic do indeed show that the pellet induces a change in radial electric field as expected by the decrease in toroidal rotation velocity [32].

In experiments to study the pellet effect on the plasma edge, it was observed in DIII-D that transitions from L- to H-mode can be spontaneously triggered by pellets injected from both the HFS and LFS [33], effectively lowering the H-mode threshold power by more than 2 MW (30%). Detailed measurements show that the transition does not require a critical edge temperature because the edge temperature is significantly lowered by the pellets. Edge fluctuations are observed to exhibit fast dithering or bursting before steady H-mode condi-

tions are achieved. The precise mechanism for the pellet-induced L- to H-mode transition is still under study.

IV. PELLET INTERACTION WITH EDGE PLASMA

Pellets injected into DIII-D H-mode plasmas from all injection locations are observed to trigger ELMs. The ELMs triggered by pellets injected from the HFS and vertical ports are similar in duration and magnitude to the background Type 1 ELMs. The ELMs triggered from the LFS outer midplane pellets are of significantly longer duration and may well be temporary transitions back to L-mode [34]. The duration of the ELM or transition back to L-mode for the LFS pellets lasts up to 30 ms and is observed in ELM-free H-mode conditions as well as ELMing H-mode. This transition back to L-mode causes a significant particle and thermal loss to the plasma.

A comparison of the ELM response to HFS and LFS pellet injection is shown in Fig. 10 for pellets injected into the same neutral beam heated H-mode plasma. The density perturbation is larger with the HFS pellet as it was in the L-mode case shown in Fig. 3. The D_α light emission in the upper divertor shows a strong increase following the pellet in the LFS injected pellet, but, the ELM triggered by the HFS injected pellet is qualitatively the same as the normal background ELMs. The magnetic loops also see a larger magnetic field perturbation from the LFS injected pellets. The reason for this difference is under investigation and is likely due to pellet induced changes in edge stability [35]; these may be different for LFS and HFS injected pellets because of the $\mathbf{E} \times \mathbf{B}$ major radius drift of the ablatant discussed in Sec. II.

V. SUMMARY AND CONCLUSIONS

Pellet injection from the HFS inner wall is found to lead to deeper mass deposition than identical pellets injected from the LFS outside midplane, in spite of a factor of 4 lower pellet speed. Accurate measurements of the pellet deposition show a strong major radius

drift that appears to play a role in the fueling from all three injection locations on DIII-D. The mechanism may be an $\mathbf{E} \times \mathbf{B}$ force on the vertically polarized ablatant that occurs from curvature and $\nabla \mathbf{B}$ drifts of the ion and electrons in the pellet ablatant cloud. Pellet injection from the HFS and vertical locations leads to improved pellet fueling depth and efficiency and is a unique enabling technology for providing new physics understanding on DIII-D.

Deep HFS pellet fueling in combination with co- and counter-NBI leads to an internal transport barrier that is similar to the PEP mode obtained on JET [15]. These DIII-D experiments are the first to use only NBI heating and the first with the radial electric field determined. Strong bootstrap current generated by a sharp pressure gradient modifies the q profile, which sustains a strong negative shear region in the plasma core. Thermal transport is reduced in the core negative shear region similar to non-PEP ITB plasmas and is consistent with $\mathbf{E} \times \mathbf{B}$ shear suppression of ITG modes. Electron particle transport is reduced even more in the core than in non-PEP ITB plasmas. The core pressure and neutron emission are diminished immediately with the onset of MHD activity, which terminates the PEP-mode.

Transitions from L- to H-mode have been triggered by pellets from both the HFS and LFS, effectively lowering the H-mode threshold power by 2.4 MW (30%). The transition does not require a critical edge temperature because the edge temperature is significantly lowered by the pellets. Pellets injected into H-mode plasmas are found to trigger ELMs. The ELMs triggered from the LFS outside midplane injected pellets are of significantly larger amplitude and longer duration than from HFS injected pellets. The rapid loss of particles from the pellet ablatant outward drift may be partially responsible for the larger ELMs induced by LFS injected pellets.

ACKNOWLEDGMENTS

The authors would like to acknowledge the support and encouragement of Drs. S. L. Milora, P. K. Mioduszewski, and T. C. Simonen.

This work was supported by the Oak Ridge National Laboratory managed by Lockheed Martin Energy Research Corp. for the U.S. Department of Energy under Contract No. DE-AC05-96OR22464 and also supported under contracts DE-AC03-99ER54463, DE-AC02-76CH03073, and DE-FC02-99ER54512.

REFERENCES

[1] S. L. Milora, W.A. Houlberg, L.L. Lengyel, V. Mertens, Nucl. Fusion **35**, 657 (1995).

[2] S. K. Combs, S.L. Milora, L.R. Baylor, C.R. Foust, F.E. Gethers, D.O. Sparks, J. Vac. Sci. Technol. **A6(3)**, 1901 (1988).

[3] L. R. Baylor, G. L. Schmidt, W. A. Houlberg, S. L. Milora, C. W. Gowers, W. P. Bailey, M. Gadeberg, P. Kupschus, J. A. Tagle, D. K. Owens, D. K. Mansfield, H. K. Park, Nucl. Fusion **32**, 2177 (1992).

[4] P. T. Lang, K. Büchl, M. Kaufmann, R. S. Lang, V. Mertens, H. W. Müller, J. Neuhauser, ASDEX Upgrade, and NI Teams, Phys. Rev. Lett. **79**, 1478 (1997).

[5] L. R. Baylor, T.C. Jernigan, C. Hsieh, Fusion Tech. **34**, 425 (1998).

[6] J. de Kloe et al., Phys. Rev. Lett. **82**, 2685 (1999).

[7] H. W. Müller, K. Büchl, M. Kaufmann, P.T. Lang, R.S. Lang, A. Lorenz, M. Maraschek, V. Mertens, J. Neuhauser, ASDEX Upgrade Team, Phys. Rev. Lett. **83**, 2199 (1999).

[8] S. K. Combs, L.R. Baylor, C.R. Foust, M.J. Gouge, T.C. Jernigan, S.L. Milora, J-F. Artaud, A. Geraud, Fusion Tech. **34**, 419 (1998).

[9] W. A. Houlberg, S. L. Milora, S. E. Attenberger, Nucl. Fusion **28**, 595 (1988).

[10] W. A. Houlberg, S. E. Attenberger, L. R. Baylor, M. Gadeberg, T. C. Jernigan, P Kupschus, S. L. Milora, G. L. Schmidt, D. W. Swain, M. L. Watkins, Nucl. Fusion **32**, 1951 (1992).

[11] P.B. Parks, Plasma Phys. Control. Fusion **38**, 571 (1996).

[12] L.R. Baylor, T.C. Jernigan, C. Hsieh, R. Maingi, A. Mahdavi, J. Nucl. Matl. **266**, 457 (1999).

[13] V. Rozhansky, I. Veselova, S. Voskoboynikov, Plasma Phys. Control. Fusion **37**, 399

(1995).

[14] P.B. Parks, W.D. Sessions, L.R. Baylor, to be published in Phys. of Plasmas **7**, (2000).

[15] The JET Team (G.L. Schmidt), Plasma Physics and Controlled Nuclear Fusion Research, (Proc. 12th Int. Conf. Nice, 1988), IAEA Vienna, 215 (1989).

[16] B.J.D. Tubbing, B. Balet, D.V. Bartlett, C.D. Challis, S. Corti, R.D.Gill, C. Gormezano, C.W. Gowers, M. von Hellermann, M. Hugon, J.J. Jacquinot, H.Jaekel, P. Kupschus, K. Lawson, H. Morsi, J.O'rourke, D. Pasini, F.G. Rimini, G. Sadler, G.L. Schmidt, D.F.H. Start, P.M. Stubberfield, A.Tanga, F.Tibone, Nucl. Fusion **31**, 839 (1991).

[17] C. M. Greenfield, D. P. Schissel, B. W. Stallard, E. A. Lazarus, G. A. Navratil, K. H. Burrell, T. A. Casper, J. C. DeBoo, E. J. Doyle, R. J. Fonck, C. B. Forest, P. Gohil, R. J. Groebner, M. Jakubowski, L. L. Lao, M. Murakami, C. C. Petty, C. L. Rettig, T. L. Rhodes, B. W. Rice, H. E. St. John, G. M. Staebler, E. J. Strait, T S. Taylor, A. D. Turnbull, K. L. Tritz, R. E. Waltz, and the DIII-D Team, Phys. Plasmas **4**, 1596 (1997).

[18] M. Greenwald et al., Phys. Rev. Lett. **53**, 352 (1984).

[19] L. R. Baylor, G. L. Schmidt, S. H. Batha, M. G. Bell, M. Bitter, E. D. Fredrickson, G. W. Hammett, D. L. Jassby, F. C. Jobes, F. M. Levinton, R. Majeski, R. Nazikian, D. K. Owens, H. K. Park, C. K. Phillips, A. I. Ramsey, J. H. Rogers, S. A. Sabbagh, G. Schilling, J. E. Stevens, E. J. Synakowski, G. Taylor, J. R. Wilson, Nucl. Fusion **37**, 127 (1997).

[20] P. Gohil, K.H. Burrell, R.J. Groebner, in *Fusion Technology 2*, Proceedings 14th Symposium, San Diego, California, 1991 (Institute of Electrical and Electronic Engineers, New York, 1992), p.1199.

[21] L. L. Lao, J. R. Ferron, R. J. Groebner, W. Howl, H. St. John, E. J. Strait, and T. S. Taylor, Nucl. Fusion **30**, 1035 (1990).

[22] B. W. Rice, K.H. Burrell, L. L. Lao, Nucl. Fusion **37**, 517 (1998).

[23] R. J. Hawryluk, *in Proceedings of the Course of Plasmas Close in Thermonuclear Conditions*, Varenna, 1979 (Commission of the European Communities, Brussels, 1980), Vol. I, p 19.

[24] W. A. Houlberg, Phys. Plasmas 4, 3230 (1997).

[25] D. R. Ernst, M. G. bell, R. E. Bell, C. E. Bush, Z. Chang, E. Fredrickson, L. R. Grisham, K. W. Hill, D. L. Jassby, D. K. Mansfield, D. C. McCune, H. K. Park, A. T. Ramsey, S. D. Scott, J. D. Strachan, E. J. Synakowski, G. Taylor, M. Thompson, and R. M. Wieland, Phys. Plasmas **5** 665 (1998).

[26] K. H. Burrell, Phys. Plasmas 4, 1499 (1997).

[27] B. W. Stallard, C. M. Greenfield, G.M. Staebler, C. L. Rettig, M. S. Chu, M. E. Austin, D. R. Baker, L. R. Baylor, K. H. Burrell, J. C. DeBoo, J. S. deGrassie, E. J. Doyle, J Lohn, G. R. McKee, R. L. Miller, W. A. Peebles, C. C. Petty, R. I. Pinsker, B. W. Rice, T. L. Rhodes, R. E. Waltz. L. Zeng, and the DIII-D Team, Phys. of Plasmas **6**, 1978 (1999).

[28] C. M. Greenfield et al., and the DIII-D Team, to be published in Phys. Plasmas **7**, (2000).

[29] M. Kotschenreuther, G. Rewoldt, W.M. Tang, Comput. Phys. Commun. **88**, 128 (1995).

[30] R.L. Miller, M.S. Chu, J.M. Greene, Y.R. Lin-Liu, R.E. Waltz, Phys. Plasmas **5**, 973 (1998).

[31] L. A. Charlton, L. R. Baylor, W. A. Houlberg et al., Nucl. Fusion **31**, 1835 (1991).

[32] P. Gohil, K.H. Burrell, L.R. Baylor, T.C. Jernigan, Bull. Am. Phys. Soc. **43**, 1959 (1998).

[33] L.R. Baylor, P. Gohil, K.H. Burrell, T.C. Jernigan, W.A. Houlberg, Czech. J. of Phys.

49, Suppl. S3, (1999).

[34] P. Gohil, K.H. Burrell, L.R. Baylor, T.C. Jernigan, to be published in Bull. Am. Phys. Soc. **44**, (1999).

[35] R. Maingi, M. A. Mahdavi, T. C. Jernigan, R. J. La Haye, A. W. Hyatt, L. R. Baylor, D. G. Whyte, M. R. Wade, T. W. Petrie, J. W. Cuthbertson, A. W. Leonard, M, Murakami, R. T. Snider, R. D. Stambaugh, J. G. Watkins, W. P. West, and R. D. Wood, Phys. Plasmas **4**, 1752 (1997).

[36] J. R. Ferron, et al., and the DIII-D Team, to be published in Phys. Plasmas **7**, (2000).

FIGURES

FIG. 1. The pellet injection locations on DIII-D shown in a poloidal cross section. The HFS ports are at different toroidal locations from the V+1 and LFS ports.

FIG. 2. The line average electron density evolution and D_α emission in the upper divertor for 2.7 mm pellets injected from the LFS, V+1, and HFS locations in a 4.5 MW neutral beam heated L-mode plasma in an upper single null configuration.

FIG. 3. The measured particle deposition of a 2.7 mm pellet injected from the HFS 45 inner wall tube compared with a pellet injected from the LFS outside midplane in the same discharge. The calculated penetration depths for these pellets are shown as vertical arrows.

FIG. 4. The measured net pellet deposition profile from a 2.7 mm pellet injected from the inner wall (HFS 45) overlayed with the measured pellet light emission mapped onto flux surface geometry and calculated deposition profile from the PELLET code NGS model.

FIG. 5. The temporal evolution of the key parameters in a typical PEP-mode ITB discharge. A pellet is injected from the LFS during the current rise followed in 20 ms by a HFS injected pellet at 0.6 s. The density evolution for a comparison non-PEP ITB plasma is also shown for reference.

FIG. 6. Profiles of the (a) electron density, (b) electron and ion temperature and q profile for the PEP-mode plasma shown in Fig. 5. The density profile for the non-pellet ITB comparison is also shown.

FIG. 7. (a) The bootstrap current density profiles from NCLASS calculation in TRANSP for a PEP ITB and non-PEP ITB comparison discharge. (b) The q profile derived from MSE data by the EFIT equilibrium code.

FIG. 8. Transport analysis results for the PEP-mode disharge (solid) of Fig. 5 compared with a non-PEP ITB comparison discharge (dotted) showing (a) ion thermal diffusivity, (b) electron thermal diffusivity, and (c) electron particle diffusivity.

FIG. 9. (a) Measured carbon toroidal velocity profiles for co- and counter-NBI PEP-mode cases. The calculated toroidal velocity profile from NCLASS for the main ion species in the co-NBI case is shown as the dashed curve. (b) The calculated radial electric field profiles for the co-NBI case and (c) counter-NBI case using the measured carbon rotation and pressure profiles.

FIG. 10. GKS predictions for ITG mode stability for a PEP-mode plasma. The growth rate $\gamma_{\max}$ for the ITG and TEM modes and the ω_{ExB} flow shear rate are shown (shaded region is ITG stable).

FIG. 11. Details of ELM behavior in ELMing H-mode for a HFS injected pellet and LFS injected pellet. The line average density and divertor D_α light emission for (a) a HFS injected pellet and (b) a LFS injected pellet in the same discharge.

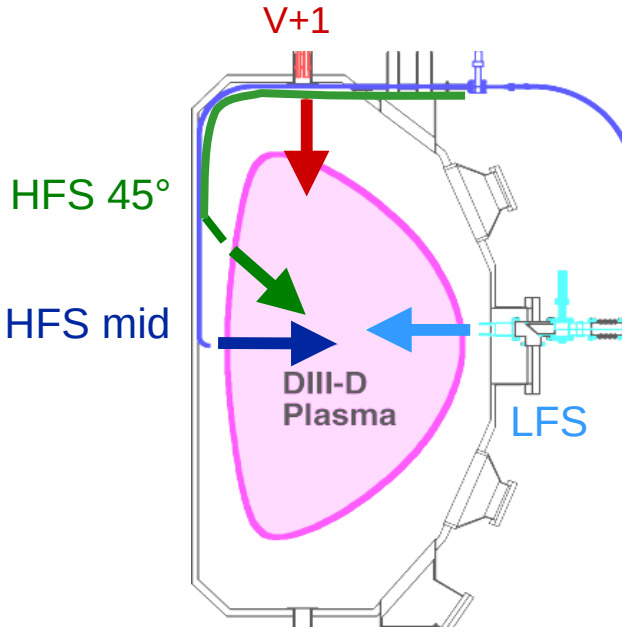

Fig. 1

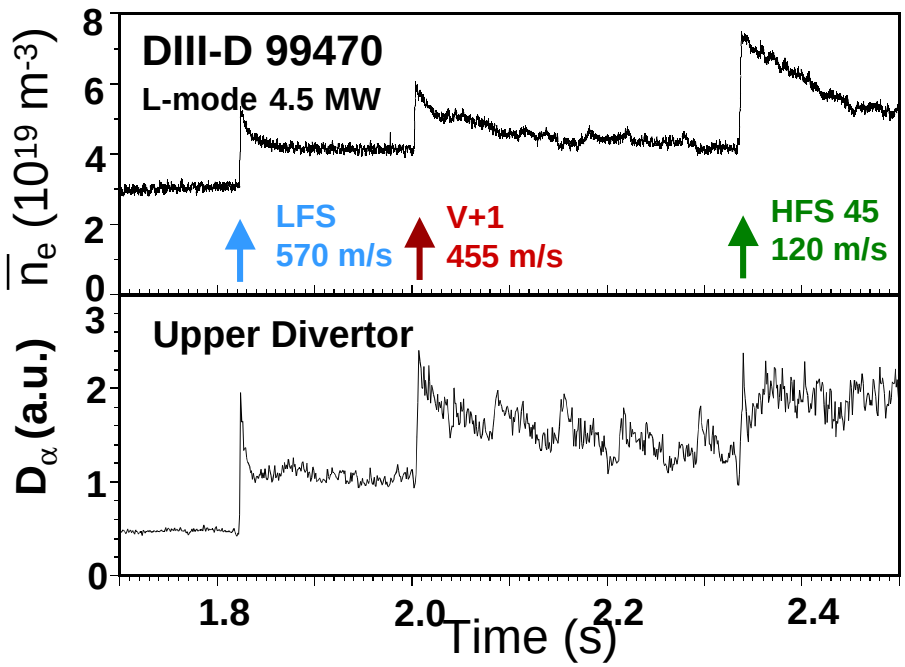
DIII-D 99470
L-mode 4.5 MW
LFS
570 m/s
V+1
455 m/s
HFS 45
120 m/s
Upper Divertor
$\overline{n}_e$ (10^{19} m^{-3})
D_α (a.u.)
Time (s)
0
2
4
6
8
1
3
1.8
2.0
2.2
2.4

Fig. 2

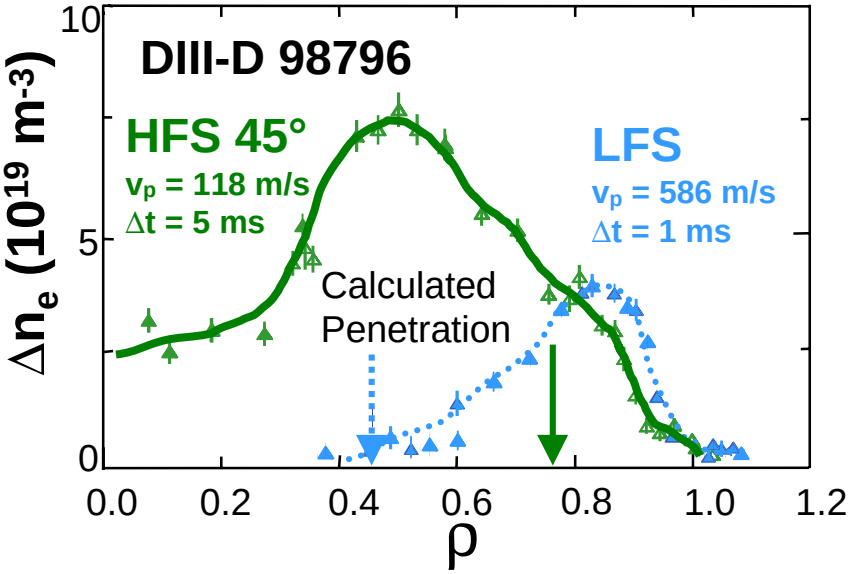
DIII-D 98796
HFS 45°
v_p = 118 m/s
Δt = 5 ms
LFS
v_p = 586 m/s
Δt = 1 ms
Calculated
Penetration
Δn_e (10^{19} m^{-3})
ρ
0
5
10
0.0
0.2
0.4
0.6
0.8
1.0
1.2

Fig. 3

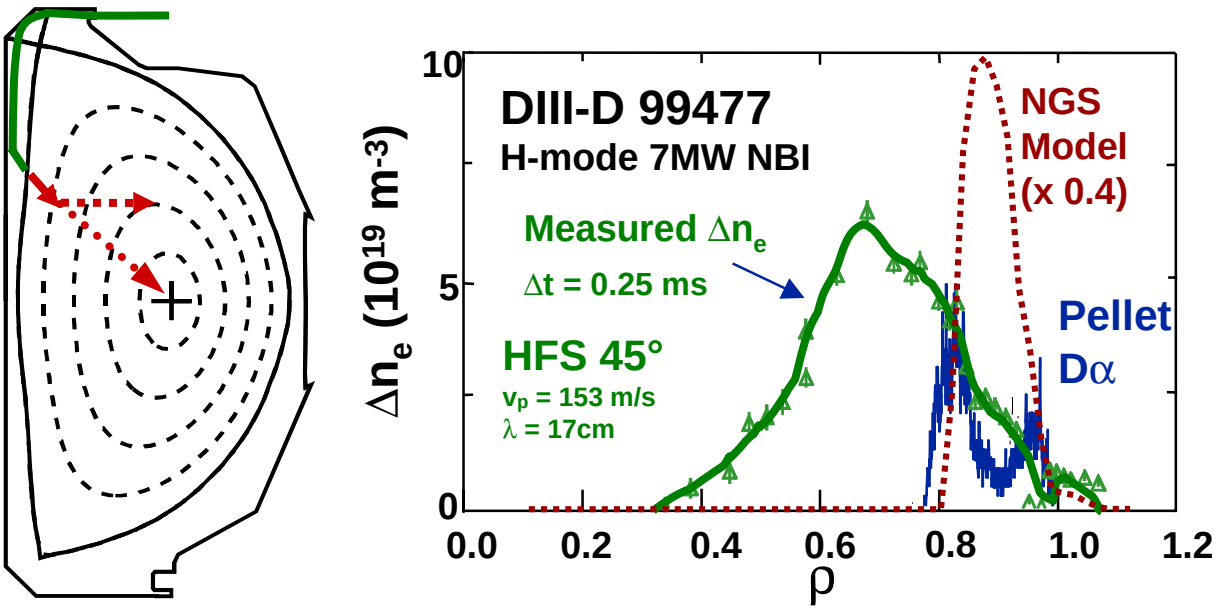
DIII-D 99477
H-mode 7MW NBI
Measured Δne
Δt = 0.25 ms
HFS 45°
vp = 153 m/s
λ = 17cm
NGS
Model
(x 0.4)
Pellet
Dα
Δne (10^19 m^-3)
ρ
0
5
10
0.0
0.2
0.4
0.6
0.8
1.0
1.2

Fig. 4

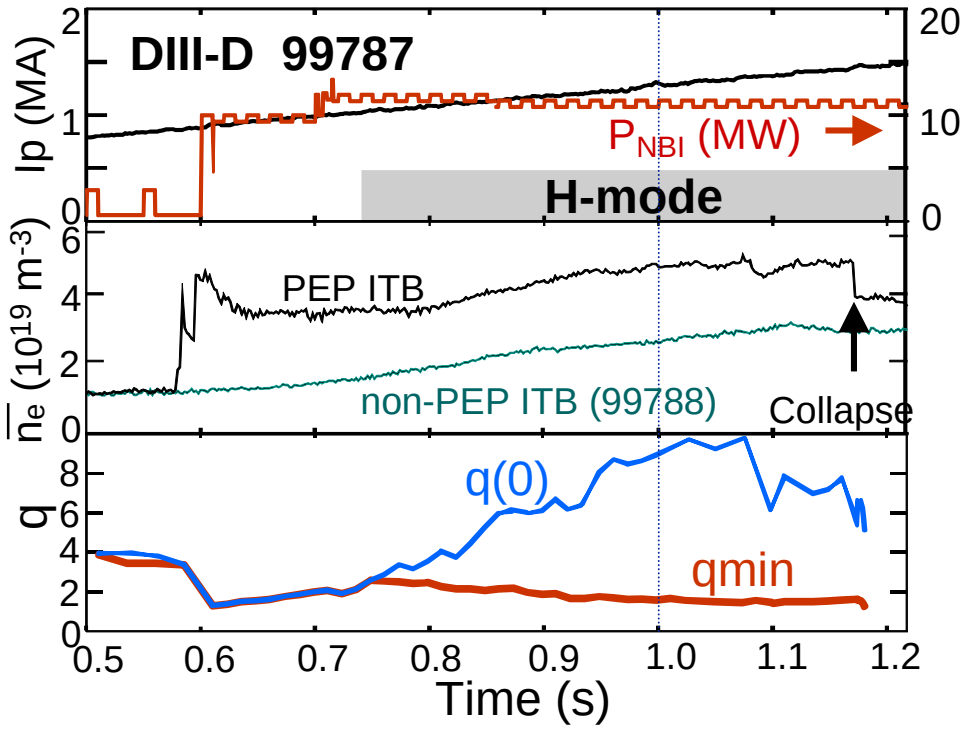
DIII-D 99787
Ip (MA)
P_{NBI} (MW)
H-mode
PEP ITB
non-PEP ITB (99788)
Collapse
$\overline{n}_e$ (10^{19} m^{-3})
q(0)
qmin
q
Time (s)

Fig. 5

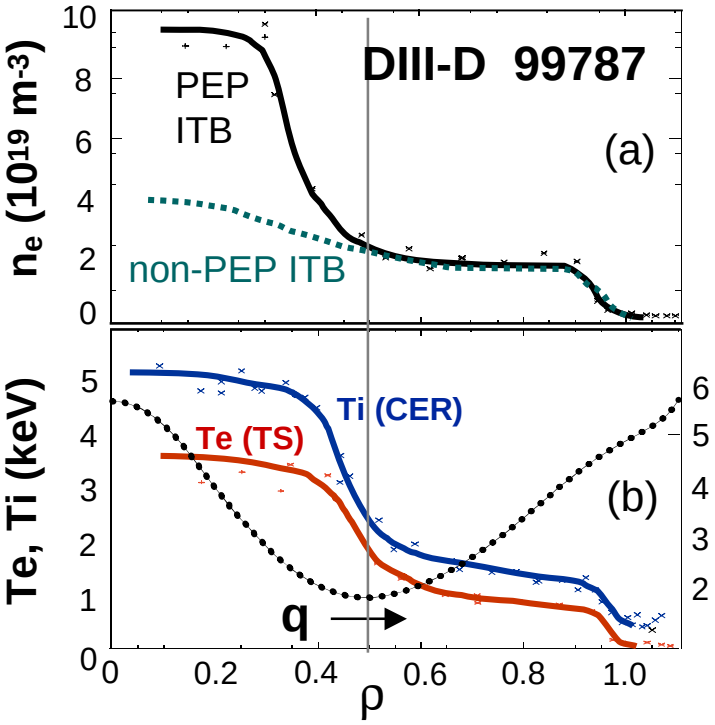
DIII-D 99787
PEP
ITB
(a)
non-PEP ITB
n_e (10^{19} m^{-3})
Ti (CER)
Te (TS)
(b)
q
Te, Ti (keV)
ρ
0
0.2
0.4
0.6
0.8
1.0

Fig. 6

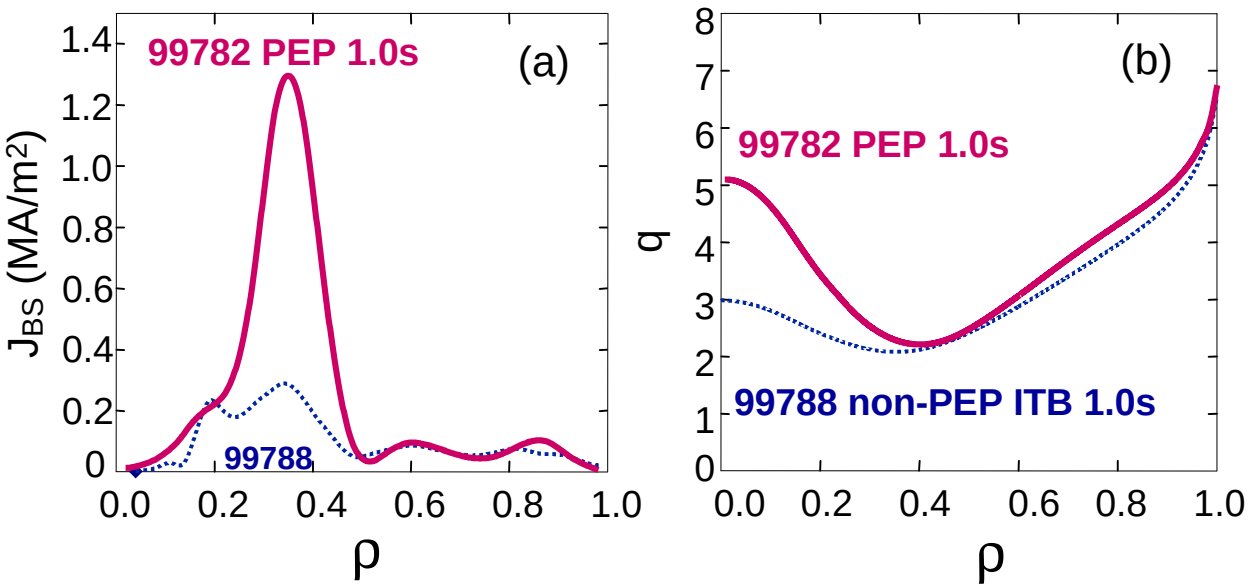
99782 PEP 1.0s
(a)
99788
J_{BS} (MA/m^2)
ρ
(b)
99782 PEP 1.0s
99788 non-PEP ITB 1.0s
q
ρ

Fig. 7

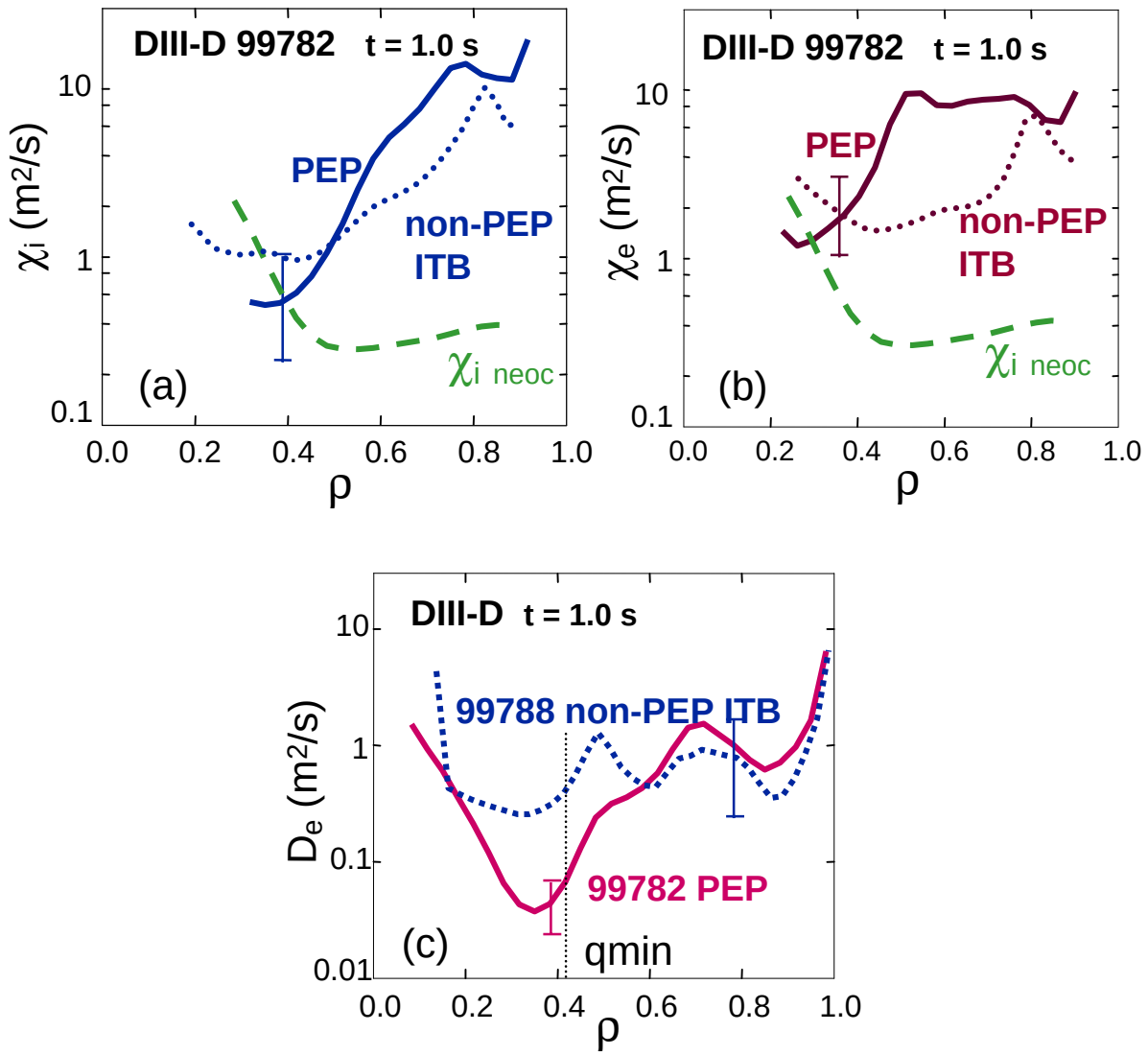
DIII-D 99782 t = 1.0 s
PEP
non-PEP
ITB
χi neoc
(a)
χi (m2/s)
ρ
DIII-D 99782 t = 1.0 s
PEP
non-PEP
ITB
χi neoc
(b)
χe (m2/s)
ρ
DIII-D t = 1.0 s
99788 non-PEP ITB
99782 PEP
qmin
(c)
De (m2/s)
ρ

Fig. 8

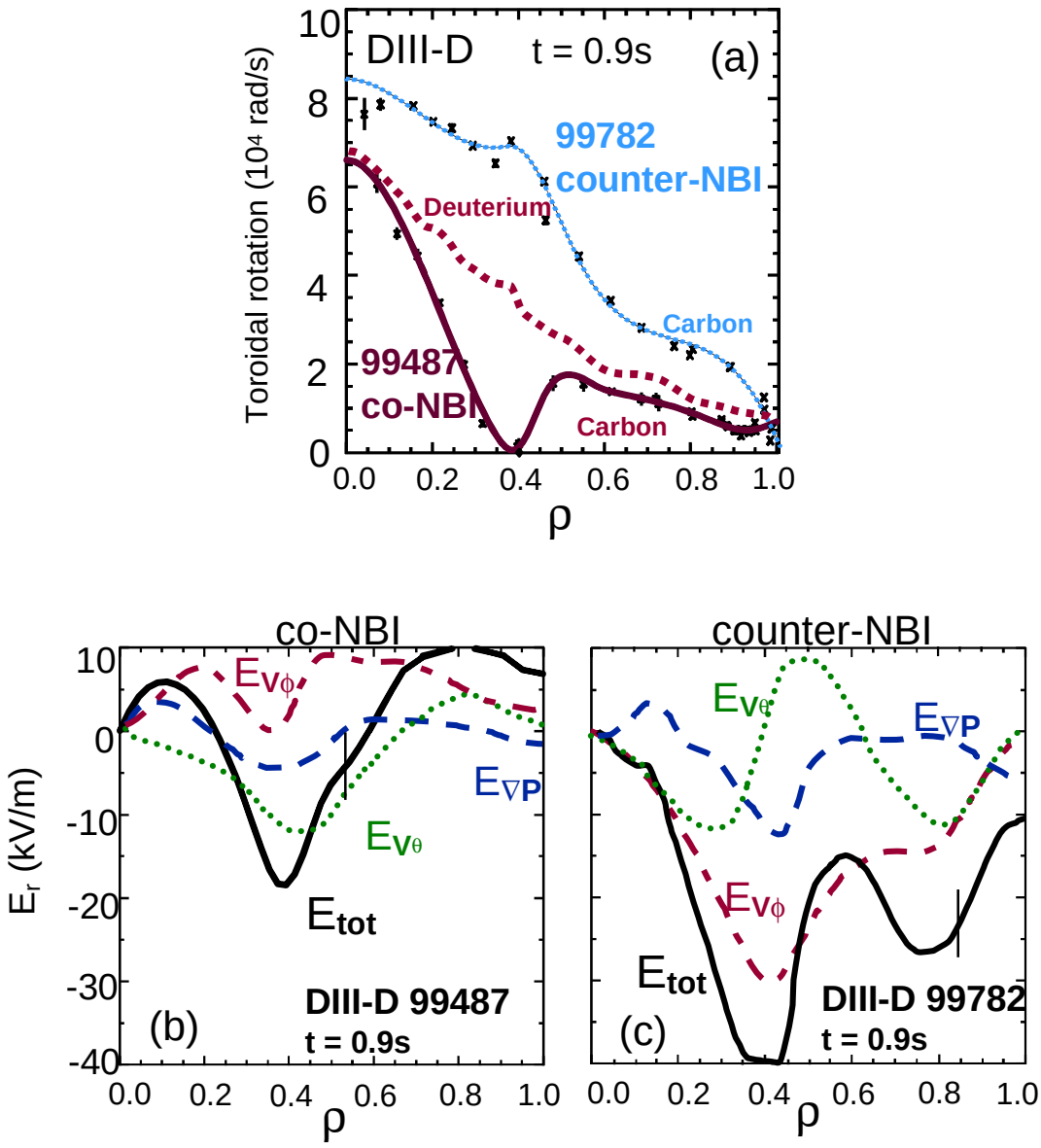
DIII-D
t = 0.9s
(a)
99782
counter-NBI
Deuterium
Carbon
99487
co-NBI
Carbon
Toroidal rotation (10^4 rad/s)
ρ
co-NBI
counter-NBI
$E_{v\phi}$
$E_{\nabla P}$
$E_{v\theta}$
E_{tot}
E_r (kV/m)
DIII-D 99487
t = 0.9s
(b)
DIII-D 99782
t = 0.9s
(c)

Fig. 9

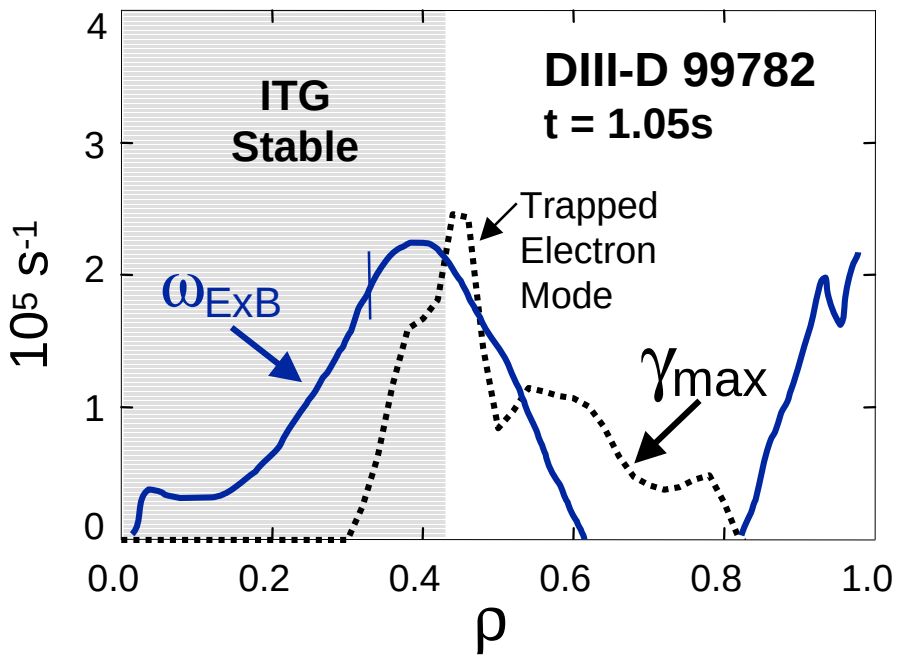
DIII-D 99782
t = 1.05s
ITG
Stable
Trapped
Electron
Mode
ωExB
γmax
10^5 s^-1
ρ
0
1
2
3
4
0.0
0.2
0.4
0.6
0.8
1.0

Fig. 10

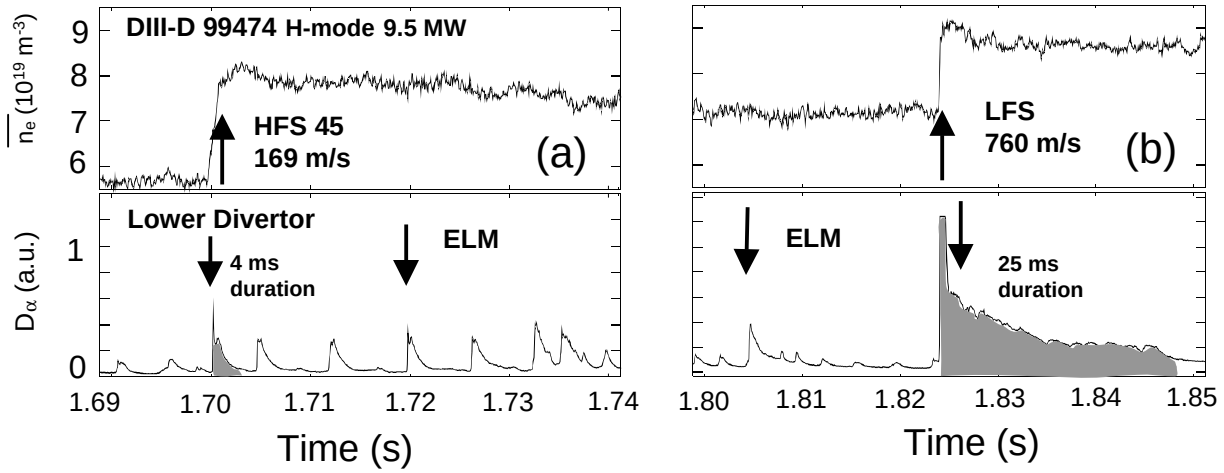
DIII-D 99474 H-mode 9.5 MW
$\overline{n_e}$ (10^{19} m^{-3})
9
8
7
6
HFS 45
169 m/s
(a)
LFS
760 m/s
(b)
Lower Divertor
4 ms
duration
ELM
ELM
25 ms
duration
D_α (a.u.)
1
0
1.69
1.70
1.71
1.72
1.73
1.74
1.80
1.81
1.82
1.83
1.84
1.85
Time (s)
Time (s)

Fig. 11